

Return of 4U 1730–22 after 49 years silence: the peculiar burst properties of the 2021/2022 outbursts observed by Insight-HXMT

Yu-Peng Chen*

chenyp@ihep.ac.cn

Key Laboratory for Particle Astrophysics, Institute of High Energy Physics, Chinese Academy of Sciences, 19B Yuquan Road, Beijing 100049, China

Shu Zhang*

szhang@ihep.ac.cn

Key Laboratory for Particle Astrophysics, Institute of High Energy Physics, Chinese Academy of Sciences, 19B Yuquan Road, Beijing 100049, China

Long Ji*

jilong@mail.sysu.edu.cn

School of Physics and Astronomy, Sun Yat-Sen University, Zhuhai, 519082, China

Shuang-Nan Zhang

Key Laboratory for Particle Astrophysics, Institute of High Energy Physics, Chinese Academy of Sciences, 19B Yuquan Road, Beijing 100049, China

University of Chinese Academy of Sciences, Chinese Academy of Sciences, Beijing 100049, China

Peng-Ju Wang

Key Laboratory for Particle Astrophysics, Institute of High Energy Physics, Chinese Academy of Sciences, 19B Yuquan Road, Beijing 100049, China

University of Chinese Academy of Sciences, Chinese Academy of Sciences, Beijing 100049, China

Ling-Da Kong

Key Laboratory for Particle Astrophysics, Institute of High Energy Physics, Chinese Academy of Sciences, 19B Yuquan Road, Beijing 100049, China

*Institut für Astronomie und Astrophysik, Kepler Center for Astro and Particle Physics,
Eberhard Karls Universität, Sand 1, D-72076 Tübingen, Germany*

Zhi Chang

*Key Laboratory for Particle Astrophysics, Institute of High Energy Physics, Chinese
Academy of Sciences, 19B Yuquan Road, Beijing 100049, China*

Jing-Qiang Peng

*Key Laboratory for Particle Astrophysics, Institute of High Energy Physics, Chinese
Academy of Sciences, 19B Yuquan Road, Beijing 100049, China*

*University of Chinese Academy of Sciences, Chinese Academy of Sciences, Beijing 100049,
China*

Qing-Cang Shui

*Key Laboratory for Particle Astrophysics, Institute of High Energy Physics, Chinese
Academy of Sciences, 19B Yuquan Road, Beijing 100049, China*

*University of Chinese Academy of Sciences, Chinese Academy of Sciences, Beijing 100049,
China*

Jian Li

*CAS Key Laboratory for Research in Galaxies and Cosmology, Department of Astronomy,
University of Science and Technology of China, Hefei 230026, China*

*School of Astronomy and Space Science, University of Science and Technology of China,
Hefei 230026, China*

Zhao-Sheng Li

*Key Laboratory of Stars and Interstellar Medium, Xiangtan University, Xiangtan 411105,
Hunan, P.R. China*

Lian Tao

*Key Laboratory for Particle Astrophysics, Institute of High Energy Physics, Chinese
Academy of Sciences, 19B Yuquan Road, Beijing 100049, China*

Ming-Yu Ge

Key Laboratory for Particle Astrophysics, Institute of High Energy Physics, Chinese Academy of Sciences, 19B Yuquan Road, Beijing 100049, China

Jin-Lu Qu

Key Laboratory for Particle Astrophysics, Institute of High Energy Physics, Chinese Academy of Sciences, 19B Yuquan Road, Beijing 100049, China

University of Chinese Academy of Sciences, Chinese Academy of Sciences, Beijing 100049, China

ABSTRACT

After in quiescence for 49 years, 4U 1730–22 became active and had two outbursts in 2021 & 2022; ten thermonuclear X-ray bursts were detected with Insight-HXMT. Among them, the faintest burst showed a double-peaked profile, placing the source as the 5th accreting neutron star (NS) exhibiting double/triple-peaked type-I X-ray bursts; the other bursts showed photospheric radius expansion (PRE). The properties of double-peaked non-PRE burst indicate that it could be related to a stalled burning front. For the five bright PRE bursts, apart from the emission from the neutron star (NS) surface, we find the residuals both in the soft (<3 keV) and hard (>10 keV) X-ray band. Time-resolved spectroscopy reveals that the excess can be attributed to an enhanced pre-burst/persistent emission or the Comptonization of the burst emission by the corona/boundary-layer. We find, the burst emission shows a rise until the photosphere touches down to the NS surface rather than the theoretical predicted constant Eddington luminosity. The shortage of the burst emission in the early rising phase is beyond the occlusion by the disk. We speculate that the findings above correspond to that the obscured part (not only the lower part) of the NS surface is exposed to the line of sight due to the evaporation of the obscured material by the burst emission, or the burst emission is anisotropic ($\xi > 1$) in the burst early phase. In addition, based on the average flux of PRE bursts at their touch-down time, we derive a distance estimation as 10.4 kpc.

Subject headings: stars: coronae — stars: neutron — X-rays: individual (4U 1730–22) — X-rays: binaries — X-rays: bursts

1. Introduction

Until June of 2022, there were three outbursts observed from 4U 1730–22: lasting ~ 6 months in 1972 detected by Uhuru (Cominsky et al. 1978; Forman et al. 1978), lasting 1 month in 2021 and lasting 3 months in 2022, and all three with peak flux of 100 mCrab in soft X-ray band. In the interval between the first two outbursts, a bright X-ray emission in its quiescent state was observed by Chandra, which indicates its neutron star’s (NS) nature (Tomsick et al. 2007) and its distance estimation of ~ 10 kpc. In the 2nd outburst, 49 years after the 1st one, thermonuclear bursts were detected in 4U 1730–22 by NICER, which identified as NS X-ray binary (Li et al. 2022). Its spin is around $\nu=584.65$ Hz (Li et al. 2022), based on the burst oscillation detection by NICER.

Type-I X-ray bursts, also named thermonuclear X-ray bursts, are triggered by unstable thermonuclear burning of the accumulated accretion fuel from a low-mass X-ray binary (LMXB) hosting a NS (for reviews, see Lewin et al. 1993; Cumming 2004; Strohmayer & Bildsten 2006; Galloway et al. 2008). Bursting behavior is known to be extremely variable and violent, and most bursts manifest as a fast-rise (seconds), an exponential decay (~ 10 s to minutes) and a peak luminosity up to the Eddington luminosity. Most bursts are single-peaked, except the brightest ones which show photospheric radius expansion (PRE; due to radiation pressure).

For the PRE bursts, the radiation pressure of the burning exceeds the NS gravitational force in the photosphere, resulting in an increase of the photosphere radius and a decrease of the photosphere temperature in an adiabatic expansion; as the expansion ceases, the lifted photosphere drops on the NS surface and an increase of the photosphere temperature is shown in an adiabatic compression (Grindlay et al. 1980).

The above spectral shift causes a dip in the temperature, a spike in the radius and a plateau in the luminosity in the PRE phase. In the lightcurves, a single-peaked structure is typically observed with soft X-ray instruments, e.g., RXTE/PCA, Swift/XRT, Chandra, XMM-Newton, NICER and Insight-HXMT/LE, but a double-peaked structure is often seen with hard X-ray instruments because of the passband limitation, e.g., INTEGRAL, Swift/BAT, RXTE/HEXTE and Insight-HXMT/HE.

The vast majority of the bursts with luminosity below the Eddington limit show a single peak in the lightcurves. Non-PRE bursts with double-peaked or triple-peaked structures have been detected in four bursters, e.g., 4U 1636–536 (Bhattacharyya & Strohmayer 2006; Zhang et al. 2009), 4U 1608–52 (Penninx et al. 1989; Güver et al. 2021), GX 17+2 (Kuulkers et al. 2002), and GRS 1741.9–2853 (Pike et al. 2021). Potential explanations include multiple generations/release of thermonuclear energy, absorption/scattering from an

accretion-disk corona, and flame spread stalling on the NS surface (e.g., ignites at high latitude but stalls on the equator; Pike et al. 2021).

Since the bursts occur on the NS surface, the interplay between the NS surface emission and the accretion environment should be taken into account. In recent ten years, among thousands of observed bursts from the 118 bursters¹, impacts observed on the accretion process by bursts have been observed, i.e., an enhancement/deficit (Worpel et al. 2013, 2015; Bult et al. 2021; Ji et al. 2014) at soft X-ray band, a shortage at hard X-ray band (Maccarone & Coppi 2003; Chen et al. 2012; Ji et al. 2013), a bump peaking at 20–40 keV and/or discrete emission by reflection from accretion disk (in’t Zand et al. 2013; Ballantyne & Strohmayer 2004; Keek et al. 2014).

In this work, using a broad energy band capabilities of Insight-HXMT in 1–50 keV, we study ten bursts from 4U 1730–22: one double-peaked burst and nine PRE bursts. The present paper focuses on the nature of these bursts and also examines the effect of the burst emission on the accretion environment using a variable persistent flux method and Comptonization of the burst emission by the surrounding hot electrons. We describe the observations and data reduction in Section 2, present our analysis methods, spectral results on outburst and spectral/temporal properties of the bursts in Section 3. Finally, a discussion and understanding of the above results are given in Section 4.

2. Observations and Data Reduction

2.1. Insight-HXMT

Hard X-ray Modulation Telescope (HXMT, also dubbed as Insight-HXMT, Zhang et al. 2020) excels in its broad energy band (1–250 keV) and a large effective area in the hard X-rays energy band. It carries three collimated telescopes: the High Energy X-ray Telescope (HE; poshwich NaI/CsI, 20–250 keV, $\sim 5000 \text{ cm}^2$), the Medium Energy X-ray Telescope (ME; Si pin detector, 5–40 keV, 952 cm^2) and the Low Energy X-ray telescope (LE; SCD detector, 1–12 keV, 384 cm^2). Under the quick read-out system of Insight-HXMT detectors, there is little pile-up effect at the burst peak. Insight-HXMT Data Analysis software (HXMTDAS) v2.05² is used to analyze the data.

¹<https://personal.sron.nl/~jeanz/bursterlist.html>

²<http://hxmtweb.ihep.ac.cn/>

As shown in Figure 1, for the two outbursts in 2021 and 2022, Insight-HXMT have observed 4U 1730–22 with 74 observations ranging from P041401100101-20210707-01-01 to P051400201402-20220513-02-01 with a total observation time of 184 ks. These observations covered the peak/decay phase of the outburst in 2021 and the plateau of the outburst in 2022.

We note that the default good-time-interval (GTI) selection criteria of LE are very conservative because of the influence of light leaks. To obtain a complete sample of bursts, lightcurves are extracted without filtering GTIs. Burst-like fluctuations that may be caused by a sharp variation of the background, when the telescope passes the South Atlantic Anomaly (SAA), are excluded.

As shown in Table 1, 10 bursts are found in ME and HE data with a peak flux ~ 300 – 600 cts/s and ~ 100 – 200 cts/s; among them, 6 bursts are also found in LE data with a peak flux ~ 300 – 1200 cts/s.

For each burst, we use the time of the ME flux peak as a reference (0 s in Figure 3) to produce lightcurves and spectra. We extract time-resolved spectra of LE, ME and HE with a bin size of 0.5 s starting from the onset of each burst. As a conventional procedure, the pre-burst emission (including the persistent emission and the instrumental background) is extracted, which is taken as the background when fitting the spectra during bursts. In practice, for each burst, we define the time interval between 70 and 20 seconds before the burst peak as the time window of the pre-burst emission, i.e., [-70 s, -20 s].

For the outburst in 2022, the last eight bursts locates at the plateau of the outburst. In this period, the overlapped observations between Insight-HXMT and NICER are P051400200102-20220430-01-01 and 4639010134, respectively. Thus, we get 600 s and 2300 s GTI of LE and ME. The HE spectrum is not involved in the joint spectral fitting of the persistent emission, since the HE detection falls below the systematic error of the background model. Please notice that the HE spectra are involved in the bursts analysis, since the peak fluxes of the burst detected by HE are much brighter than the persistent emission.

The other results, e.g, the persistent spectra, background and net lightcurves are obtained following the recommended procedure of the Insight-HXMT Data Reduction, which are screened with the standard criterion included in Insight-HXMT pipelines: lepipeline, mepipeline and hepipeline.

For the persistent emission spectral fitting of LE and ME, the energy bands are chosen to be 2–7 keV and 8–20 keV. The spectra are rebinned by ftool ftgrouppha (Kaastra & Bleeker 2016) optimal binning algorithm with a minimum of 25 counts per grouped bin.

The LE background model works only in a certain temperature range (Li et al. 2020). This leads to some uncertainties below 2 keV caused by the electronic noise when the temperature exceeds this range after the middle year of 2019. During a burst with a time-scale of tens of seconds, the temperature fluctuation of LE is so small that can be neglected. The resulting electronic noise of the pre-burst spectrum is the same as that of burst spectra. Therefore, the influence of the electronic noise can be canceled out when we take the pre-burst spectrum as the background of burst spectra. In this case, the energy band of LE can be extended to 1–10 keV in the burst analysis.

The ME and HE energy bands used in burst spectral fitting are 8–30 keV and 25–50 keV, respectively. The slices of burst spectra of LE, ME and HE are rebinned by `ftool grppha` with a minimum of 10 counts per grouped bin, based on the limited photons of the burst slice spectra due to the short exposure time. We added a systematic uncertainty of 1% to the Insight-HXMT spectra to account for the systematic uncertainties in the detector calibrations (Li et al. 2020).

2.2. NICER

For the two outbursts, NICER also performed high cadence observations on 4U 1730–22. There are two bursts during the outburst in 2021, but there is no LE data for both of them. Without the LE data, the canonical blackbody model could fit the burst spectra well, and there is no need for adding another component during the fitting, e.g., the variable persistent emission. Under this condition, only the persistent spectra of the outburst in 2022 are extracted for fitting, and the derived parameters of the model is used to fit the burst spectra.

There are several NICER observations in the plateau of the outburst of 2022, and we choose an overlapped obsid of 4639010134 (Table 2) to joint fit the spectra of Insight-HXMT and NICER. The observation has a GTI ~ 450 s and a count rate ~ 600 cts/s in the 0.3–12 keV band.

The NICER data are reduced using the pipeline tool `nicerl23` in NICERDAS v7a with the standard NICER filtering and using `ftool XSELECT` to extract lightcurves and spectra. The background is estimated using the tool `nibackgen3C50` (Remillard et al. 2022). The Focal Plane Module (FPM) No. 14 and 34 are removed from the analysis because of increased detector noise. The response matrix files (RMFs) and ancillary response files (ARFs) are

³https://heasarc.gsfc.nasa.gov/docs/nicer/nicer_analysis.html

generated with the `ftool nicerrmf` and `nicerarf`. The spectra are rebinned by `ftool ftgrouppha` (Kaastra & Bleeker 2016) optimal binning algorithm with a minimum of 25 counts per grouped bin.

The `tbabs` model with Wilm abundances accounts for the ISM absorption in the spectral model (Wilms et al. 2000). The resulting spectra are analyzed using XSPEC (Arnaud 1996) version 12.11.1. We added a systematic uncertainty of 1% to the NICER spectrum.

3. Analysis and Results

3.1. Fitting the joint Insight-HXMT/NICER spectrum of persistent emission

We fit the joint NICER and Insight-HXMT (LE and ME) spectra with an absorbed convolution thermal Comptonization model (with input photons contributed by the spectral component `diskbb`), available as `thcomp` (a more accurate version of `nthcomp`) (Zdziarski et al. 2020) in XSPEC, which is described by the optical depth τ , electron temperature kT_e , scattered/covering fraction f_{sc} . The hydrogen column (`tbabs` in XSPEC) accounts for both the line-of-sight column density and any intrinsic absorption near the source. The seed photons are in the shape of `diskbb` since the `thcomp` model is a convolution model, and a fraction of Comptonization photons are also given in the model. Normalization constants are included during fittings to take into account the inter-calibrations of the instruments. We keep the normalization factor of the NICER data with respect to the LE and ME data to unity.

Using the model above, we find an acceptable fit: reduced $\chi_v=0.91$ (d.o.f. 160; Figure 2 and Table 3), with the inner disc radius R_{diskbb} and temperature kT_{in} found to be $\sim 19.3_{-1.6}^{+1.9}$ km (with a distance of 10 kpc and an inclination angle of 0 degree) and $0.68_{-0.34}^{+0.39}$ keV respectively. Please note that the distance is given in the following pages based on the PRE bursts. The `thcomp` parameters of the electron temperature kT_e and optical depth τ are $3.61_{-0.57}^{+0.42}$ keV and $7.8_{-0.9}^{+1.0}$. The scattered/covering fraction f_{sc} is derived as 0.929. However, when we extract the confidence region for f_{sc} , the parameter is pegged at hard limit–1. It is then frozen at 1; as expected, the results are consistent with each other within parameter’s error bar. The derived hydrogen column density N_{H} is $0.53 \pm 0.01 \times 10^{22} \text{ cm}^{-2}$. The constants of LE and ME are 0.93 ± 0.01 and 0.83 ± 0.05 , respectively. The inferred bolometric flux in 0.01–1000 keV is $3.08_{-0.03}^{+0.04} \times 10^{-9} \text{ erg cm}^{-2} \text{ s}^{-1}$ corresponding to 20.5% L_{Edd} at distance of 10 kpc, with $L_{\text{Edd}} = 1.8 \times 10^{38} \text{ erg/s}$.

The other scenario, i.e., substituting the `diskbb` component with a blackbody component in the aforementioned convolution model, is also attempted. Taking this approach, spectral fits yield roughly the same `thcomp` parameters and reduced $\chi_v=0.93$ (the same

d.o.f.). However, the derived blackbody radius is 80 ± 3 km, which is far greater than the NS radius.

3.2. Burst lightcurves by Insight-HXMT

3.2.1. *The lightcurve of the double-peaked burst*

We show the LE/ME/HE lightcurves in Fig. 3 with a time resolution of 0.5 s. The burst profiles exhibit a typical fast rise and slow (exponential) decay in the X-ray band. For the faintest burst, burst #9, there is a double-peaked structure with an interval of ~ 10 s. Both for the lightcurves of LE and ME, the peak flux of the first sub-burst is $\sim 2/3$ of that of the second one. For HE, there is an enhancement in the lightcurve, and no dip between the two sub-bursts. The rising rate of the two sub-bursts is similar for the ME: 50 cts/s increases every 0.5 s, but the decay of the first sub-burst is much faster than the second one.

3.2.2. *The lightcurve of the PRE burst*

For the five bursts with detection of LE, bursts #3–#7, the lightcurves of LE present a single-peaked structure. Moreover, the hard X-rays (ME and HE) lag behind the soft X-rays (LE) by ~ 1 s; the peak times of the ME and HE lightcurves are consistent with each other. The brightest burst, burst #7, shows a double-peaked profile in ME and HE lightcurves, which is a typical characteristic of a PRE burst. For other bright bursts, e.g., bursts #1, #2, #4, #6, there are only hints of another spike on the onset of the burst.

3.3. Broad-band spectra of burst emission by Insight-HXMT

When we fit the burst spectra, we estimate the background using the emission before the burst, i.e., assuming the persistent emission is unchanged during the burst. To account for the effective area calibration deviation, a constant is added to the model. At the first attempt, for ME, the constant is fixed to 1, the others are variable during spectral fitting. The fits indicate that most of the constants of HE and some of the constants of LE are not convergent, owing to the low-significance data. Under this situation, the constants of LE & HE are fixed at 1 for the combined-spectral fitting.

3.3.1. *Fit the spectra of bursts by the blackbody model*

We follow the classical approach to X-ray burst spectroscopy by subtracting the persistent spectrum and fitting the net spectrum with an absorbed blackbody, as shown in Figure 4. In the decay phase, such a spectral model generally results in acceptable goodness-of-fit, with a mean reduced $\chi_v^2 \sim 1.0$ (d.o.f. 20–60). However, we note that significant residuals are shown below 3 keV and above 10 keV, as shown in Figure 10, especially for the spectra in the PRE phase with the reduced $\chi_v^2 > 1.5$ (d.o.f. 60–80).

From the fitting results by the absorbed blackbody, among the ten bursts, 9 bursts are PRE bursts with peak radii 12–40 km, peak temperatures ~ 3 keV and peak bolometric fluxes $3\text{--}5 \times 10^{-8}$ erg cm $^{-2}$ s $^{-1}$. The model parameters of the bursts without LE detection, i.e., bursts #1, #2, #8, and #10, show greater errors than that of the bursts with LE detection, which prevents us from adopting other models. A similar situation exists in the faintest burst, burst #9.

3.3.2. *Fit the spectra of bursts by the f_a model*

To reduce the residuals, we first consider the f_a model to fit the bright bursts which were detected simultaneously by LE, ME, and HE: burst #3–burst #7. Following Worpel et al. (2013) we then include an additional component for fitting the variable persistent emission. We assume that during the burst the spectral shape of the persistent emission is unchanged, and only its normalization (known as the f_a factor) is changeable. As reported earlier by RXTE and NICER, the f_a model provides a better fit than the conventional one (absorbed blackbody). We compare the above two models using the F-test. In some cases, the f_a model significantly improves the fits with a p-value $\sim 10^{-5}$.

As shown in the left panels of Figures 5, 6, 7, 8, and 9, the spectral fitting results from these two models have differences mainly around the PRE phase. By considering an additional factor f_a , the burst blackbody flux tends to slightly decrease, and the temperature becomes higher but the radius shrinks. Using the average flux of the touch-down time of the five bursts $2.92 \pm 0.11 \times 10^{-8}$ erg/cm 2 /s, and assuming the empirical Eddington luminosity of 3.8×10^{38} erg/s (Kuulkers et al. 2003), we derive the source distance of 10.4 kpc. For simplicity, we use a distance of 10 kpc to calculate the luminosity and blackbody radius.

The f_a factor reaches a maximum of 6 ± 1 when the radius reaches its peak. During the PRE phase, the radius is up to ~ 30 km, which is four times larger than the radius measured at touch-down time ~ 8 km (assuming a distance of 10 kpc). This is typical of a moderate photospheric expansion.

3.3.3. *Fit the spectra of bursts by the convolution thermal Comptonization model*

Since the burst photons could also be affected by the corona/boundary-layer, we thus check if the model used in the persistent emission could be the same as the burst emission. By taking the pre-burst emission as background emission, the burst spectra are fitted by the model $\text{tbabs}^*\text{thcomp}^*\text{bb}$, in which the thcomp parameters are fixed at the persistent emission fit results. Thus the convolution thermal Comptonization model (with an input seed photon spectrum of blackbody) has the same d.o.f as the canonical blackbody model, and a more d.o.f. than the f_a model. The bb and thcomp represent the burst emission from the NS photosphere and a corona/boundary-layer influence on the burst emission. This model allows us to evaluate the contribution from both the up-scattered by the corona/boundary-layer and direct photons from the NS surface.

As shown in the right panels of Figures 5, 6, 7, 8, and 9, in the PPE phase, this model provides the best fit and yields physically acceptable spectral parameters; the obtained best-fit parameters are given in the right panels. We find that this convolved thermal-Comptonization model provides equally good results as the f_a model. As mentioned above, the free/unfixed parameters include the blackbody temperature kT_{bb} and the normalization N_{bb} . The trend of the parameters is similar to the f_a model, but with a greater change. Compared to the f_a model results, the maximum radius R_{bb} is up to $83.7^{+10.4}_{-8.2}$ km, the minimum temperature kT_{bb} is lowered to 0.81 ± 0.05 keV. Using the f_a model, the source distance is estimated as 11.2 kpc with the average flux of $2.51 \pm 0.08 \times 10^{-8}$ erg/cm²/s derived at the touch-down time of the five bursts, from the convolved thermal-Comptonization model. Other scenarios, i.e., burst reflection by the disk, NS atmosphere model $\text{carbatm}/\text{hatm}$ (Suleimanov et al. 2011, 2012, 2018) in Xspec, are also tried to fit the burst spectra, as we did in Chen et al. (2019). However, neither could alleviate the residuals at soft X-ray and hard X-ray bands simultaneously.

3.3.4. *No cooling between the sub-bursts of the double-peaked burst*

As shown in Figure 4, for the first sub-burst of the double-peaked burst, the temperature and the radius of the blackbody reach 1.9 ± 0.1 keV and 9.5 ± 1.4 km. After that, the radius drops but the temperature stays at a high value: we average the eight data points (4 seconds) during the flux dip, and get an average temperature of 1.9 ± 0.1 keV and an average radius of 5.5 ± 0.6 km. For the second sub-burst, it reaches peak flux up to 30 percent brighter than the first one.

3.4. Rising bolometric flux during the PRE phase

In Figure 11, we explore the relation between the bolometric flux, F_{bb} , and the blackbody temperature, kT_{bb} , using the parameters derived from the f_a model for the five bursts. If the whole NS surface emits as a single-temperature blackbody and a constant color correction factor, the burst flux F should scale as T_{bb}^4 in the flux-temperature diagram, and the slope represents the emitting area in the double logarithmic coordinates (Güver et al. 2012). The diagram for the convolution thermal Comptonization model is not given, since the trend is very similar with the f_a model. The diagonal line in the plot represents the line of constant radius, $R_{\text{bb}}=6.9$ km, assuming a distance $d=10$ kpc to the source, which is derived from the fitting of the decay phase of the bright burst (burst #7) in the diagram of F_{bb} vs T_{bb} by a model $F_{\text{bb}} \propto R_{\text{bb}}^2 T_{\text{bb}}^4$.

From the diagram, in the decay phase (gray points in Figure 11), it is apparent that the bursts follow the expected relation $F_{\text{bb}} \propto R_{\text{bb}}^2 T_{\text{bb}}^4$. In the PRE phase, i.e., the photospheric radius larger than the NS radius (blue points in Figure 11), the bursts depart from the $F_{\text{bb}} \propto R_{\text{bb}}^2 T_{\text{bb}}^4$ relation and locate at the left of the line of $R_{\text{bb}}=6.9$ km, which indicates larger radii. There are two junctions between the blue points and the red line: the upper one corresponds to the touch-down time, and the lower one corresponds to the time when the photosphere is just lifted from the NS surface. We notice that the fluxes of the two junctions are different, i.e., the upper one is at least twice bright as the lower one, e.g. the two fluxes for burst #3 are 0.7×10^{-8} erg/cm²/s and 2×10^{-8} erg/cm²/s, which should be the same value since both of them are the values of the Eddington limit.

4. Discussion

In this work, we have presented a spectral analysis of ten bursts and persistent emission from 4U 1730–22 in its 2021 and 2022 outbursts observed by NICER and Insight-HXMT. For the persistent emission in the outburst of 2022, the joint spectra are well fitted by an absorbed convolution thermal-Comptonization model, almost the whole of the disk emission is up-scattered by the corona, or the boundary-layer (BL), or the spreading-layer (SL). The faintest burst shows a double-peaked structure and no cooling in the interval between the two sub-bursts. For the PRE bursts, the X-ray burst shows a significant spectral deviation/excess both at < 3 keV and > 10 keV from an absorbed blackbody in the PRE phase. The residuals could be flattened by the f_a model and the convolution thermal Comptonization model. For the PRE bursts, the bolometric flux of touch-down time is about twice brighter than that of the rising part of the PRE phase.

4.1. Stalled propagation of the hot-spot during the faint burst

The faint burst, burst #9, which is not a PRE burst, does not adhere to the canonical fast-rise and exponential-decay structure of most type-I X-ray bursts, instead showing a double-peaked structure. As the bolometric flux and radius exhibit the same double-peaked profile, the temperature instead shows a plateau between the two sub-bursts. These features are different from the double-peaked burst with about 1 s or 4 s dips with an amplitude of 25% or 40% detected from 4U 1608–52 in 1984 (Penninx et al. 1989) and 2017 (Güver et al. 2021), or the double-peaked burst with the radius increasing monotonically with time from GRS 1741.9–2853 (Pike et al. 2021) and 4U 1636–536 (Bhattacharyya & Strohmayer 2006), or the double-peaked burst with the temperature decreasing monotonically with time during the interval of the two sub-bursts from GX 17+2 (Kuulkers et al. 2002), or the triple-peaked burst with a temperature dip during the interval of the sub-bursts (Zhang et al. 2009).

Since there is an absence of temperature dip, but with a dip in the radius between the two sub-bursts, it is natural to consider that it is due to a stalled propagation of the hot-spot, which still burns in the stalled location, e.g., ignites on high latitude and stalls in the equator.

It may also be a failed PRE burst, since the sum of the two peaks has a count rate comparable to that of the PRE. In such a scenario, the entire power is released in two steps: first by the partially burning fuel, leading to the preceding sub-burst, and then by the burning of the entire NS surface.

4.2. Evidence of obscured NS surface during outbursts

In theory, for the PRE bursts, there are at least two moments that the hot spot just covers the whole NS surface: the photosphere lift-up point and the touch-down point (Shaposhnikov et al. 2003). Because of the fast rise on the onset of PRE bursts, especially most of them with a large portion of helium, which causes a much shorter time-scale of the rising phase; the latter is usually used to derive the NS radius, but the former is hard to be used to derive the NS radius due to the short rising time, i.e., the rising time is too short to accumulate enough photons for a spectral fitting, e.g., PRE bursts of XTE J1701–462 (Lin et al. 2009) detected by RXTE.

Assuming the photosphere emission is isotropic, the Eddington luminosity measured by a distant observer is dependent on the burning material, effective temperature and radius of the photosphere, e.g., Equation 7 by Galloway et al. (2008). Based on this equation, for the pure helium burning at the NS surface, i.e., at just the lift-up time and the touch-down time

of the photosphere, the observed bolometric flux should be the same. In the PRE phase, the flux observed should be higher than the above two values due to the redshift correction, e.g., the observed bolometric flux with $R=30$ km is $\sim 20\%$ higher than that with $R=10$ km. In the observations of the time-resolved spectral of the PRE bursts (Galloway et al. 2008), the vast majority of the peak flux reached a (local) maximum close to the time of peak radius, which does follow the equation above.

The above results are based on the assumption that the emission is isotropic, e.g., absence from obscuration by the accretion disk or Comptonization by the corona. However, in theory, Poynting-Robertson drag could drain the inner-accretion-disk by taking away the momentum of the accretion matter hence enlarging the local accretion rate (in't Zand et al. 2013; Worpel et al. 2013, 2015), which is faster than it is being refilled (Stahl et al. 2013; Fragile et al. 2020). Assuming that a dynamical evolution of the disk geometry causes this phenomenon, i.e., the lower NS hemisphere which is obscured before the burst (the burst PRE phase) and appears from the disk after the burst-disk interaction, as shown in Figure 1 of Shaposhnikov et al. (2003) and Figure 7 of Chen et al. (2022), the inclination angle is derived from the equation $\frac{F_{\text{rise}}}{F_{\text{decay}}} = (1 + \cos i)/2$ (Shaposhnikov et al. 2003; Shaposhnikov & Titarchuk 2004), in which F_{rise} and F_{decay} are the blackbody fluxes detected at the rising phase and decaying phase, respectively.

However, in this case, for the bright bursts #3, #4, #6, #7, the ratio $\frac{F_{\text{rise}}}{F_{\text{decay}}}$ are equal to or less 0.5, which is out of the allowed range. Since the disk could only obscure at most half of the burst emission, another structure between the NS surface and our line of sight should be considered.

For the material obscuring our line of sight, a possible source is the left-over hydrogen which is not stably burned to helium. In theory, under a higher accretion rate, i.e., $\sim 0.1-1L_{\text{Edd}}$, hydrogen accretes faster than it can be consumed by steady burning, so that helium ignites unstably in a H-rich environment (Galloway et al. 2008). Since the persistent emission when the bursts occurred is $\sim 20\%L_{\text{Edd}}$, the helium bursts are expected. The characteristic of bursts in this work does conform to the helium burning. We know that the material in the NS surface is layered, e.g., hydrogen is on the top of helium. When the bursts occur, helium is ignited in the bottom, and the short time-scale of ignition and spread prevents hydrogen ignition; instead, the top-layered hydrogen is lifted up by the radiation pressure of the helium burning. In this case, the lifted-up hydrogen blocks our line of sight and causes a flux underestimation in the rising part of the PRE phase. For the thermal emission of the lifted-up hydrogen, its temperature is the same as the temperature of the NS surface, ~ 0.5 keV, as our afterward estimation on the emission NS surface, which is too faint to be detected by Insight-HXMT.

We also notice that the decay phase obeys $F \propto kT_{\text{bb}}^4$ with the radius obtained from the touch-down time, which indicates the obscuring material is not refilled during the decay part of the burst. After the bursts, there should be an enhancement of soft X-ray emission—the thermal emission from the NS surface. Assuming the NS surface with temperature $kT_{\text{bb}}=0.5$ keV and radius $R_{\text{bb}}=6.9$ km, the enhancement of the luminosity is $1/10^3$ of the flux in the touch-down time, which is too faint to be detected. Since the following burst also shows the emission shortage during the rising PRE phase due to the obscuration, we speculate that the obscuring material has been rebuilt between the bursts.

Another possibility causing a different bolometric flux in the PRE phase is the different burning material, e.g., a larger portion of helium causes a higher bolometric flux of the Eddington limit. However, the fast-rising time scale already indicates pure helium burning in the rising phase (Lin et al. 2009), and thus a higher helium portion is not possible. Yet another possibility is that the burst emission is anisotropic ($\xi > 1$) (Kuulkers et al. 2002) in the burst early phase, i.e., only part of the NS photosphere is lifted up and the rest of the photosphere is affixed to the NS surface. To a distant observer, thus can create the illusion of all of the photosphere were lifted up. However, it is hard to explain that the flux of the burst when the photospheric radius reaches its peak is still lower than that of the touch-down time. Especially, in theory, a smaller red-shift correction when the photospheric radius reaches its peak would cause a higher flux than that of the touch-down time.

Since the effective area of the X-ray telescopes in orbit is not big enough to detect the rebuilding of the obscuring material or the process of obscuring the NS surface, a larger detection area may be satisfied by the next generation of Chinese mission of the so-called eXTP (enhanced X-ray Timing and Polarimetry mission) (Zhang et al. 2019) or by stacking the lightcurves/spectra of the interval between bursts under the circumstance of enough bursts and relatively smooth persistent emission.

4.3. Comptonization of the burst emission by the BL&SL

Regarding that the temperature and optical depth deviate from the corona’s canonical values, we prefer another corona pattern, the so-called warm layer (Zhang et al. 2000) with temperature $\sim 2\text{--}3$ keV and optical depth $\sim 5\text{--}10$, which is produced by the magnetic reconnection. The Comptonization of the burst emission by the BL/SL, by adopting the convolution model (with an input seed photon spectrum of blackbody) with the parameters derived in the persistent emission fitting, was first adopted in the burst detected from 4U 1608–52 (Chen et al. 2022). Similar to our previous work (Chen et al. 2022), the scenario is also applied to the five bursts from 4U 1730–22, resulting in an equally good fit

compared with the f_a model during the bright/PRE phase. Under this scenario, the radius of the photosphere is underestimated with the canonical blackbody model or the f_a model.

5. Summary and Conclusion

In summary, from Insight-HXMT observations on 4U 1730–22, we present here one non-PRE burst with the double-peaked profile and no cooling between the two sub-bursts, and nine PRE bursts with the flux shortage during the rising phase, which can be attributed to a stalled burning front at the equator, and occlusion by the material in our line of sight or an anisotropic emission in the burst early phase, respectively.

This work made use of the data and software from the Insight-HXMT mission, a project funded by China National Space Administration (CNSA) and the Chinese Academy of Sciences (CAS). This research has made use of data and software provided by of data obtained from the High Energy Astrophysics Science Archive Research Center (HEASARC), provided by NASA’s Goddard Space Flight Center. This work is supported by the National Key R&D Program of China (2021YFA0718500) and the National Natural Science Foundation of China under grants 11733009, U1838201, U1838202, U1938101, U2038101, 12130342, U1938107.

REFERENCES

- Arnaud K. A., 1996, in Jacoby G. H., Barnes J., eds, Astronomical Society of the Pacific Conference Series Vol. 101, Astronomical Data Analysis Software and Systems V. p. 17
- Ballantyne, D. R., & Strohmayer, T. E. 2004, ApJL, 602, L105
- Bhattacharyya, S. & Strohmayer, T. E. 2006, ApJ, 636, 121
- Bult, P., Altamirano, D., Arzoumanian, Z. et al. 2021, ApJ, 920, 59
- Chen, Y. P., Zhang, S., Zhang, S. N., et al. 2012, ApJL, 752, 34
- Chen, Y. P., Zhang, S., Zhang, S. N., et al. 2019, Journal of High Energy Astrophysics, 24, 23
- Chen, Y. P., Zhang, S., Ji, L., Zhang, S. N., et al. 2022, ApJ, 936, 46
- Cominsky, L., Jones, C., Forman, W., & Tananbaum, H. 1978, ApJ, 224, 46

- Cumming, A. 2004, *Nucl. Phys. B Proc. Suppl.*, 132, 435
- Degenaar, N., Ballantyne, D. R., Belloni, T., et al. 2018, *SSRv*, 214, 15
- Forman, W., Jones, C., Cominsky, L., et al. 1978, *ApJS*, 38, 357
- Fragile, P. C., Ballantyne, D. R., & Blankenship, A. 2020, *NatAs*, 4, 541
- Güver, T., Psaltis, D., & Zel, F. 2012, *ApJ*, 747, 76
- Galloway, D. K., Munro, M. P., Hartman, J. M., et al. 2008, *ApJS*, 179, 360
- Gilfanov, M.; Revnivtsev, M.; Molkov, S. Gilfanov et al. 2003, *A&A*, 410, 217
- Grindlay, J. E., Marshall, H. L., Hertz, P et al. 1980, *ApJL*, 240, L121
- Grebenev, S. A., & Sunyaev, R. A. 2002, *AstL*, 28, 150
- Güver, T., Boztepe, T., Göğüş, E. et al. 2021, *ApJ*, 910, 37
- in't Zand, J. J. M., Galloway, D. K., Marshall, H. L., et al. 2013, *A&A*, 553, A83
- Ji, L., Zhang, S., Chen, Y. P., et al. 2013, *MNRAS*, 432, 2773
- Ji, L., Zhang, S., Chen, Y. P., et al., 2014, *ApJ*, 791, L39
- Kaastra, J. S.; Bleeker, J. A. M. 2016, *A&A*, 587, A151
- Keek, L., Ballantyne, D. R., Kuulkers, E., & Strohmayer, T. E. 2014, *ApJL*, 797, L23
- Kuulkers, E., Homan, J., van der Klis, M et al., 2002, *A&A*, 382, 947
- Kuulkers, E., den Hartog, P. R., in 't Zand, J. J. M., et al. 2003, *A&A* 399, 663
- Lewin, W. H. G., van Paradijs, J., & Taam, R. E. 1993, *Space Sci. Rev.*, 62, 223
- Li, Z. S., Yu, W. H., Lu, Y. Q., et al. 2022, *ApJ*, 935, 123
- Li, X. B., Li, X. F., Tan, Y. et al. 2020, *JHEA*, 27, 64
- Lin, D., Altamirano, D., Homan, J. et al. 2009, *ApJ*, 699, 60
- Maccarone, T. J. & Coppi, P. S. 2003, *A&A*, 399, 1151
- Penninx W., Damen, E., Tan, J. et al. 1989, *A&A*, 208, 146
- Pike, S. N., Harrison, F. A., Tomsick, J. A. et al. 2021, *ApJ*, 918, 9

- Remillard, R. A., Loewenstein, M., Steiner, J. F. et al. 2022, *AJ*, 163, 130
- Shaposhnikov, N., & Titarchuk, L. 2004, *ApJ*, 606, L57
- Shaposhnikov, N., Titarchuk, L., Haberl, F., 2003, *ApJL*, 593, L35
- Stahl, A., Kluźniak, W., Wielgus, M., & Abramowicz, M. 2013, *A&A*, 555, A114
- Strohmayer, T., & Bildsten, L. 2006, *New views of thermonuclear bursts (Compact stellar X-ray sources)*, 113, 156
- Suleimanov, V., & Poutanen, J. 2006, *MNRAS*, 369, 2036
- Suleimanov, V., Poutanen, J., Werner, K. 2011, *A&A*, 527, A139
- Suleimanov, V., Poutanen, J., Werner, K. 2012, *A&A*, 545, A120
- Suleimanov, V., Poutanen, J., Werner, K. 2018, *A&A*, 619, A114
- Tomsick, J. A., Gelino, D. M., & Kaaret, P. 2007, *ApJ*, 663, 461
- Wilms, J., Allen, A., & McCray, R. 2000, *ApJ*, 542, 914
- Worpel, H., Galloway, D. K., & Price, D. J. 2013, *ApJ*, 772, 94
- Worpel, H., Galloway, D. K., & Price, D. J. 2015, *ApJ*, 801, 60
- Zdziarski, A. A., Szanecki, M., Poutanen, J., Gierlinski, M., & Biernacki, P. 2020, *MNRAS*, 492, 5234
- Zhang, G. B., Méndez, M., Altamirano, D., Belloni, T. M., Homan, J., 2009, *MNRAS*, 398, 368
- Zhang, S. N., et al., 2000, *Science*, 287, 1239
- Zhang, S. N., Santangelo, A., Feroci, M., et al. 2019, *Science China Physics, Mechanics & Astronomy*, Volume 62, Issue 2, article id. 29502, 25
- Zhang, S.-N., Li, T.-P., Lu, F.-J., et al. 2020, *SCPMA*, 63, 249502

Table 1: The bursts obsid and peak time of 4U 1730–22 detected by Insight-HXMT in 2021 & 2022 outbursts

No	obsid	Burst peak time	F_{peak}	E_b	PRE
		MJD	$10^{-8} \text{ erg cm}^2 \text{ s}^{-1}$	10^{-8} erg cm^2	
1	P041401100410-20210709-02-01*	59404.30775	3.4 ± 0.3	26.9 ± 1.0	Y
2	P041401100801-20210716-01-01*	59411.72027	4.6 ± 0.4	56.6 ± 1.5	Y
3	P051400200102-20220430-01-01	59699.26105	4.2 ± 0.2	30.8 ± 0.5	Y
4	P051400200402-20220503-01-01	59702.29225	3.0 ± 0.2	25.3 ± 0.4	Y
5	P051400200601-20220505-01-01	59704.34837	2.9 ± 0.2	32.7 ± 0.5	Y
6	P051400200701-20220506-01-01	59705.15499	4.2 ± 0.2	33.5 ± 0.5	Y
7	P051400200801-20220507-01-01	59706.25535	4.9 ± 0.3	42.2 ± 0.8	Y
8	P051400200902-20220508-01-01*	59707.34785	3.7 ± 0.4	27.0 ± 0.8	Y
9	P051400201003-20220509-01-01 ^d	59708.45082	1.7 ± 0.2	12.7 ± 0.4	N
10	P051400201102-20220510-01-01*	59709.33134	3.9 ± 0.4	25.5 ± 0.8	Y

* The bursts only detected by LE

^d The burst with double-peak profile

Table 2: The NICER obsid on the same day when Insight-HXMT detected burst #3

obsid	Start Time	GTI (s)
4639010134	59700.04657 (2022-05-01T01:02:20)	453

Table 3: The results of the spectral fit of the LE, ME and NICER spectra in the 0.4–20 keV range with `cons*tbabs*thcomp*diskbb`

N_{H} 10^{22} cm^{-2}	τ	kT_e keV	f_{sc}	kT_{in} keV	N_{diskbb}	χ^2_{ν}
$0.53^{+0.01}_{-0.01}$	$7.8^{+1.0}_{-0.9}$	$3.61^{+0.42}_{-0.57}$	$0.929_{-0.12}$	$0.68^{+0.39}_{-0.34}$	$370.3^{+74.0}_{-62.8}$	146.1/160

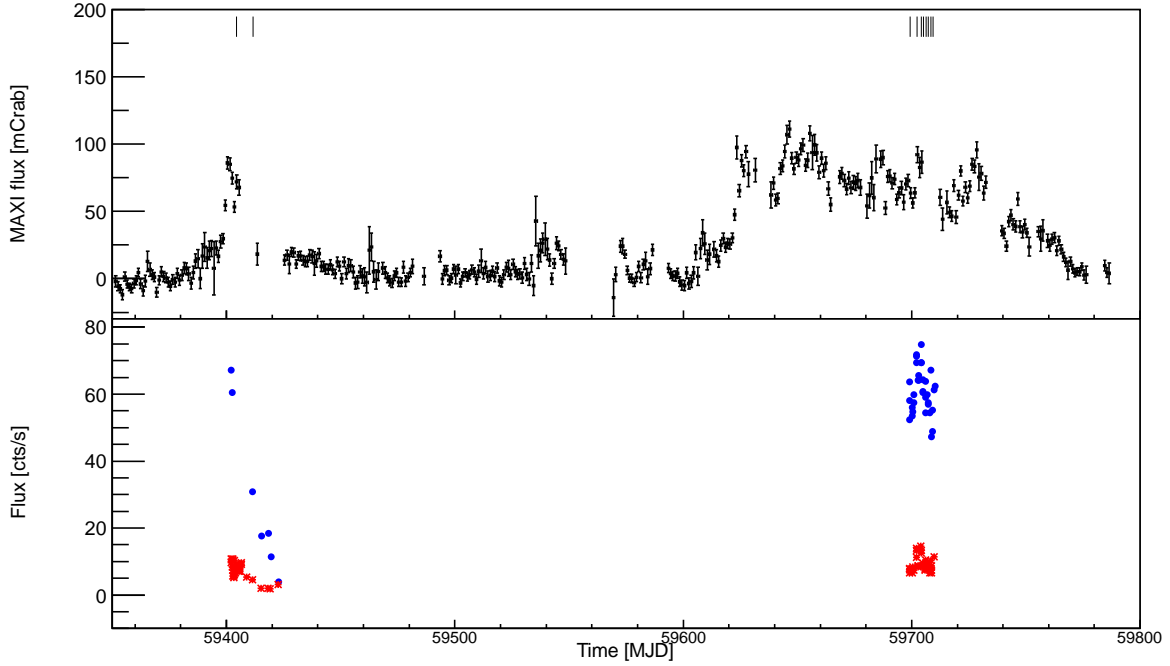


Fig. 1.— Top panel: daily light curves of 4U 1730–22 by MAXI (black) during the outbursts in 2021 and 2022 in 2–20 keV. The bursts are indicated by vertical lines. Bottom panel: light curves of 4U 1730–22 by LE (blue) and ME (red), which are rebinned by one obsid (~ 10000 s).

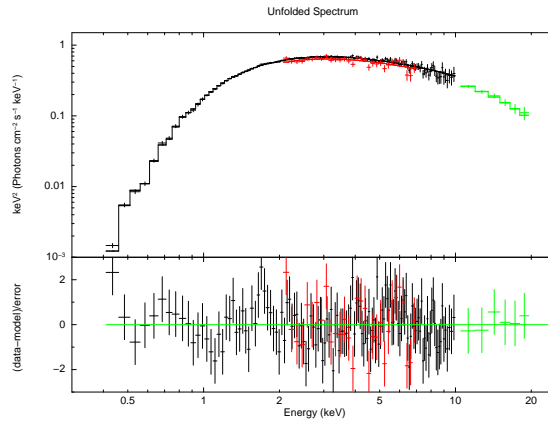


Fig. 2.— The spectral fit results of the persistent emission by NICER (black), LE (red) and ME (green) with model $\text{const}*\text{tbabs}*\text{thcomp}*\text{diskbb}$.

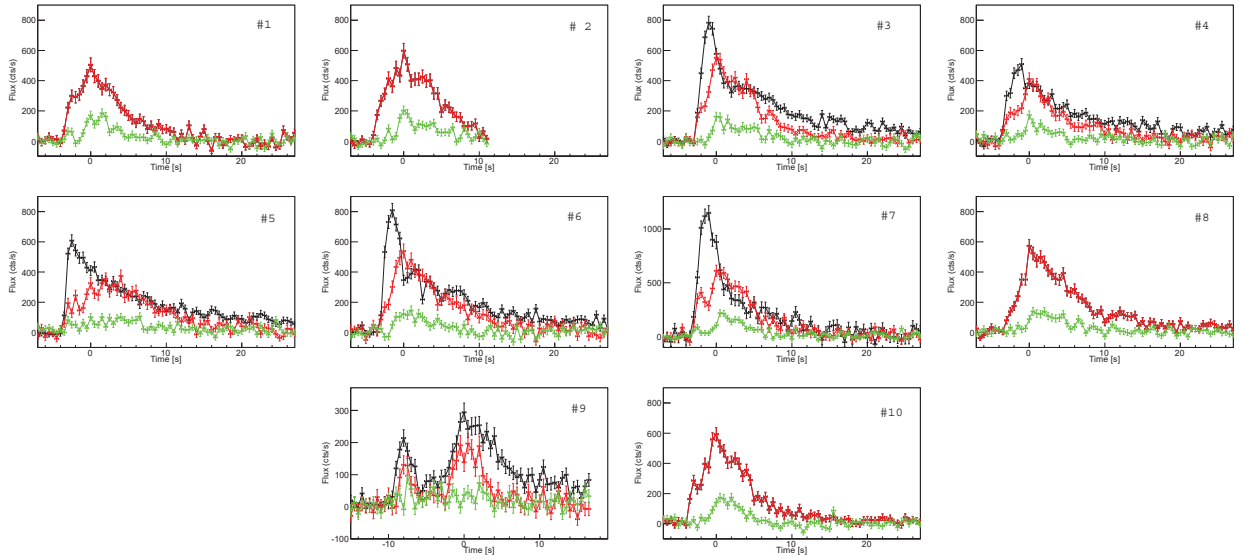


Fig. 3.— Lightcurves with pre-burst emission subtracted of the 10 type-I X-ray bursts detected in the Insight-HXMT observation of 4U 1730–22 with time bin 0.5 s by LE (black), ME (red) and HE (green). The lightcurves of LE and ME are in their full energy bands; the HE lightcurves result in 20–50 keV.

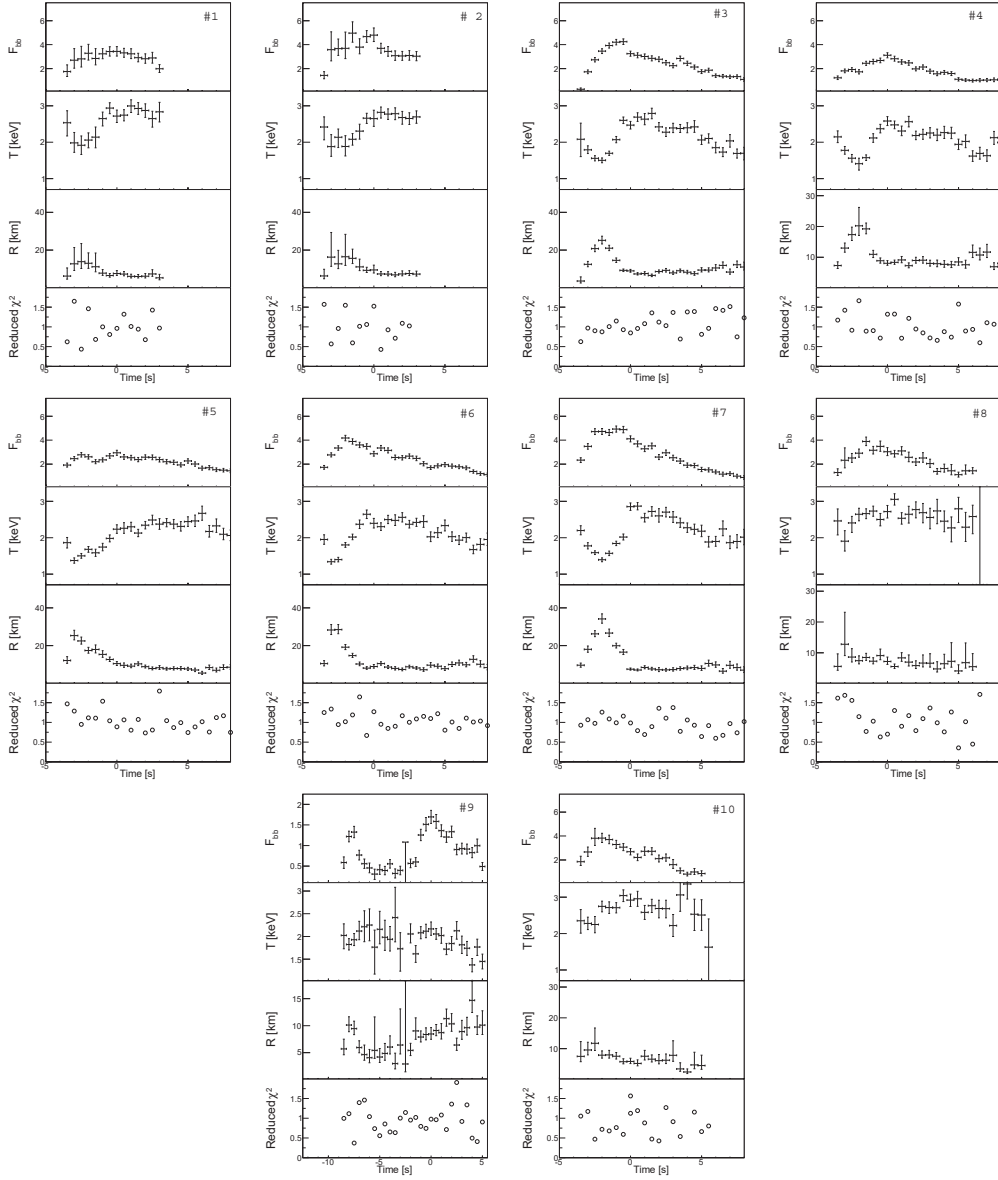


Fig. 4.— Results of the spectral fits of time-resolved spectra of the ten bursts detected from 4U 1730–22 during its 2021 and 2022 outbursts. All of the bursts except the second-to-last burst show photospheric radius expansion.

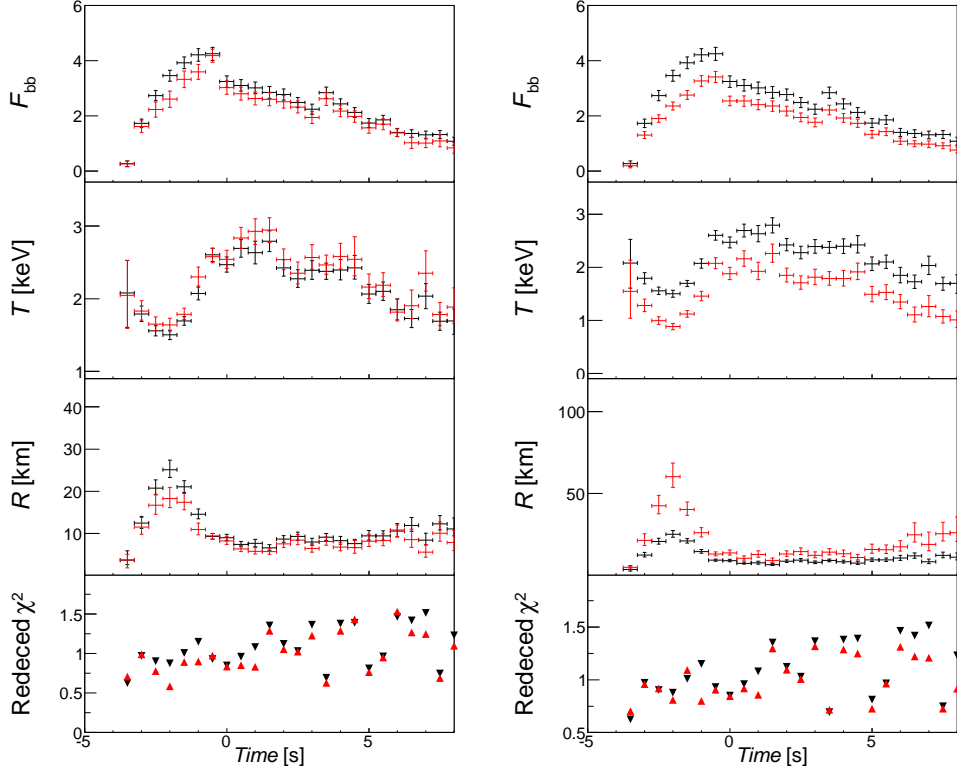


Fig. 5.— Spectral fitting result of burst #3 with time bin 0.5 second with a pure blackbody (black), f_a model (the left panel, red) and convolution thermal-Comptonization model (the right panel, red), include the time evolution of the blackbody bolometric flux F_{bb} , the temperature kT_{bb} , the observed radius R of NS surface at 10 kpc, the goodness of fit χ_v^2 . The bolometric flux of the blackbody model F_{bb} is in unit of 10^{-8} erg/cm²/s.

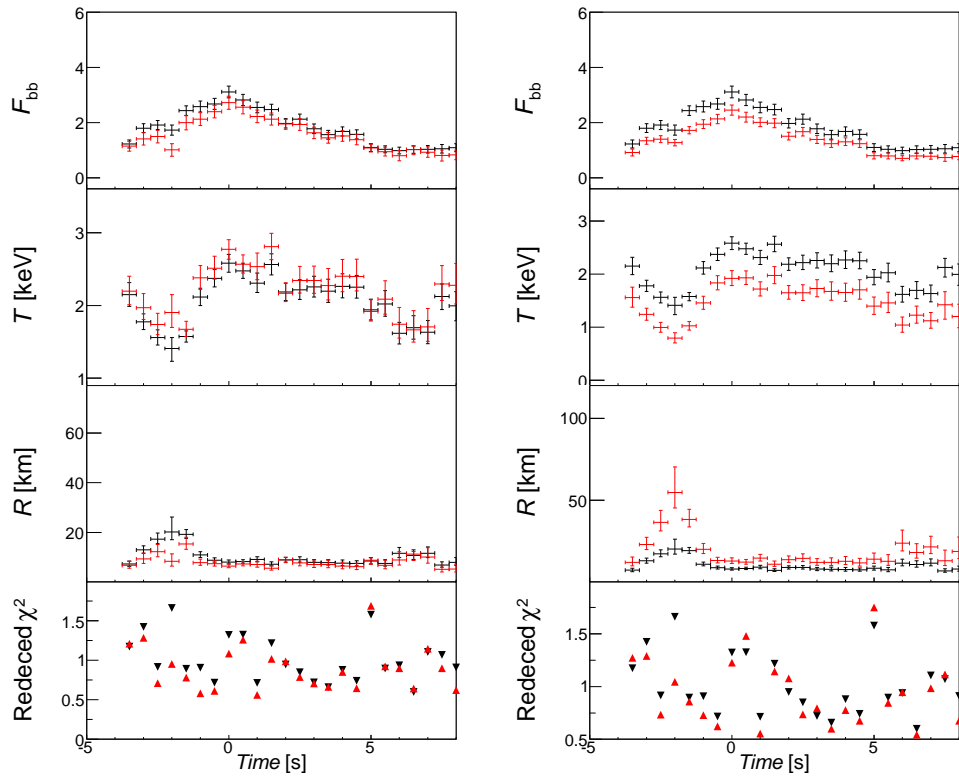


Fig. 6.— Same as Figure 5 for burst #4.

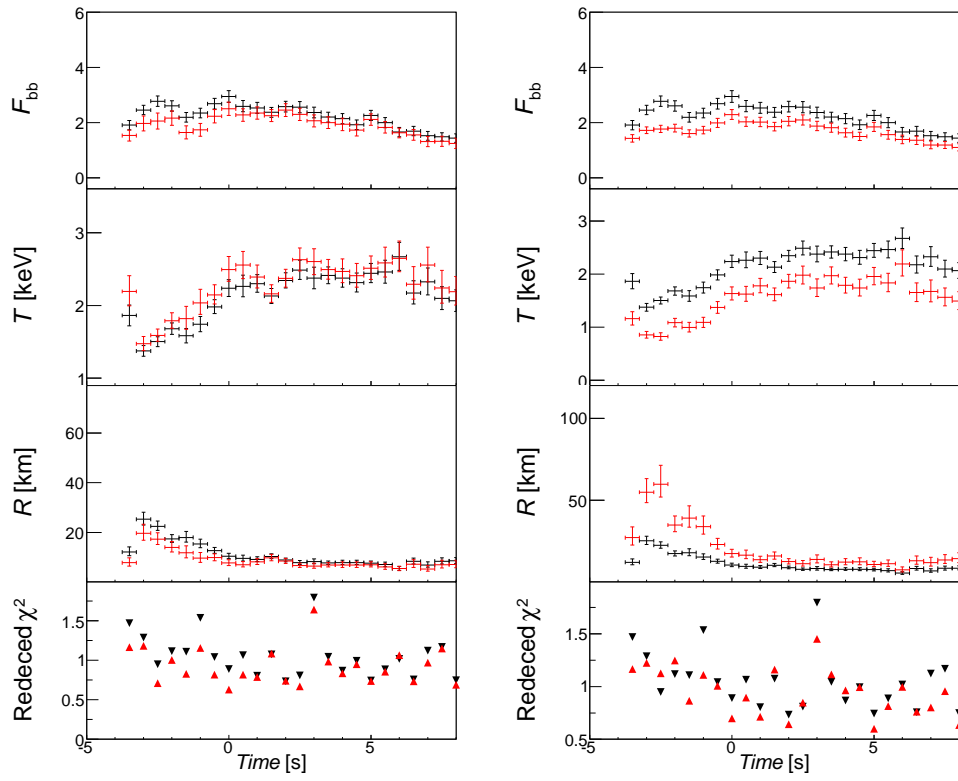


Fig. 7.— Same as Figure 5 for burst #5.

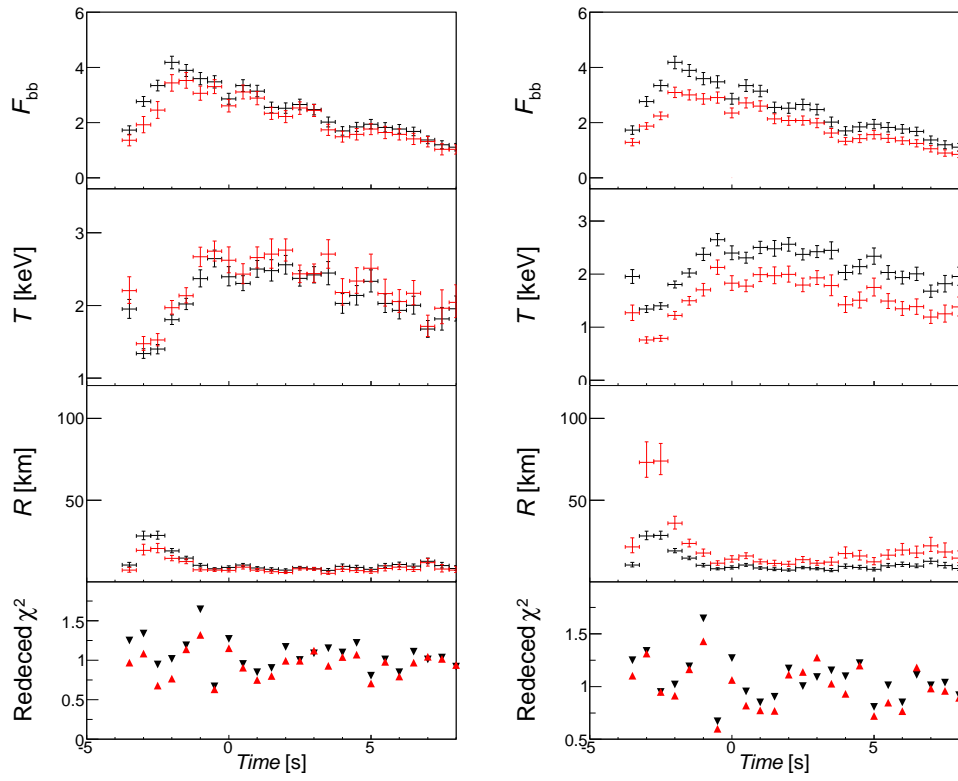


Fig. 8.— Same as Figure 5 for burst #6.

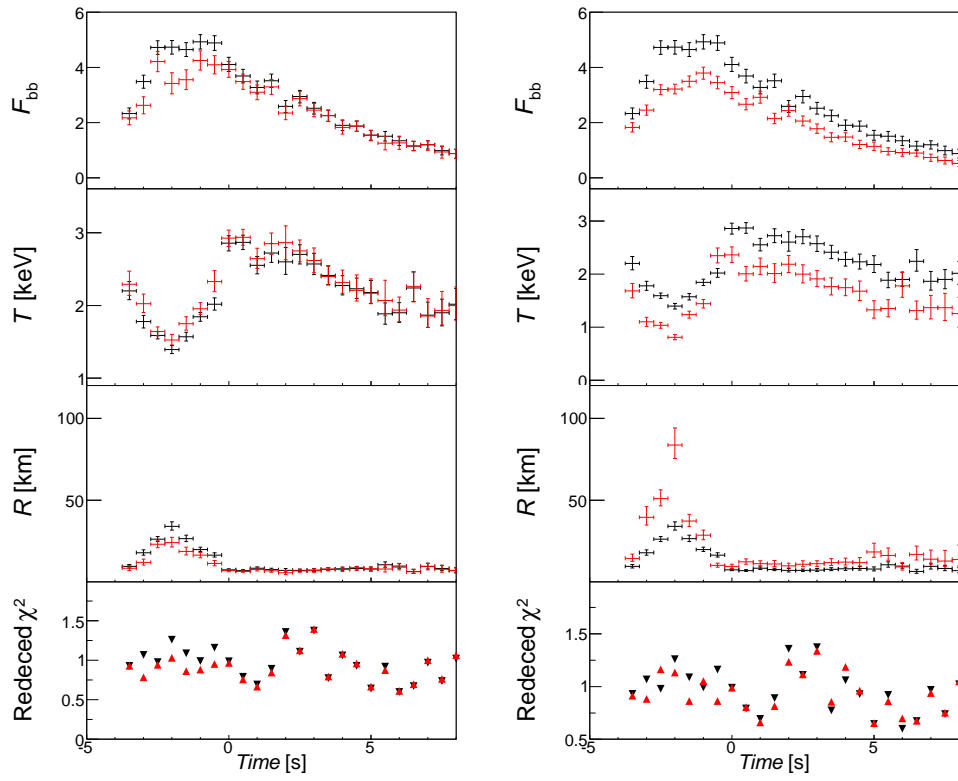


Fig. 9.— Same as Figure 5 for burst #7.

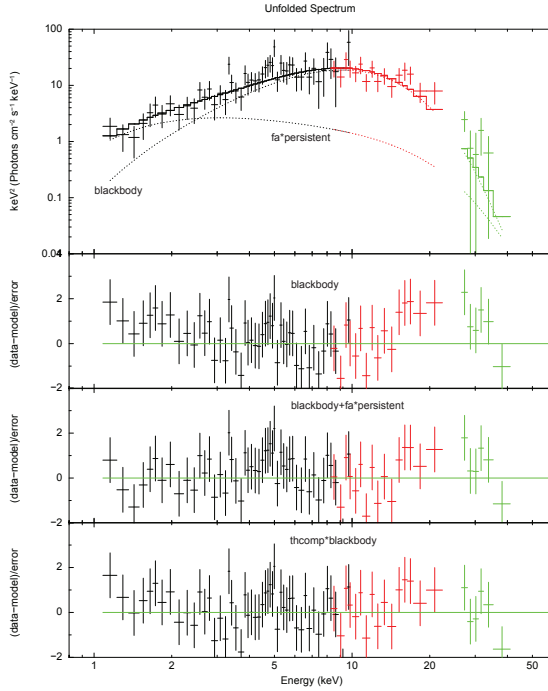


Fig. 10.— Top panel: the spectral fits results by LE (black), ME (red) and HE (green) when the burst #7 reaches the touch-down time by f_a model, the blackbody model and enhancement of the persistent emission are labeled. The three panels below: residuals of spectral fits results by an absorbed black-body model (the 2nd panel), f_a model (the 3rd panel) and convolution thermal-Comptonization model (the bottom panel).

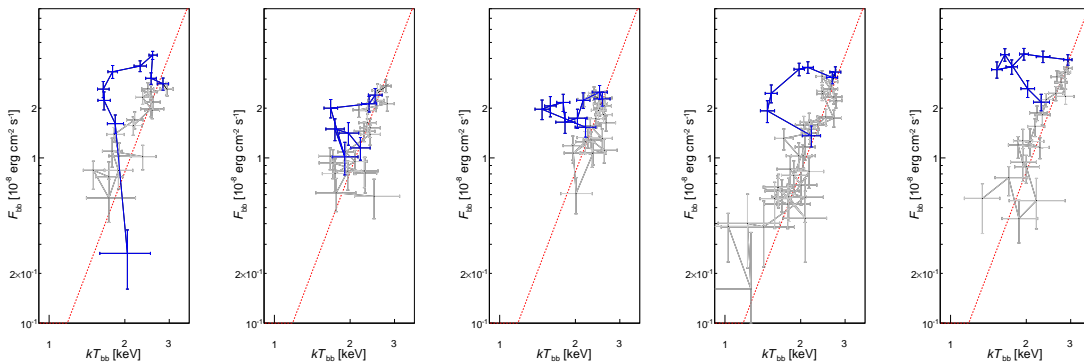


Fig. 11.— Burst flux vs. blackbody temperature of bursts #3–#7. The blue points and gray points indicate the data points before and after the touch-down times. The dashed lines correspond to $R_{BB}=6.9 \text{ km}$ under the distance of 10 kpc.